Charge-Disproportionation Symmetry Breaking Creates a Heterodimeric Myoglobin Complex with Enhanced Affinity and Rapid Intracomplex Electron Transfer

Ethan N. Trana,[†] Judith M. Nocek,[†] Jon Vander Woude,[†] Ingrid Span,[‡,§] Stephen M. Smith,[‡,∥] Amy C. Rosenzweig,[‡,†] and Brian M. Hoffman*,[†,‡]

[†]Department of Chemistry, Northwestern University, Evanston, Illinois 60208, United States
[‡]Department of Molecular Biosciences, Northwestern University, Evanston, Illinois 60208, United States

Ⓢ *Supporting Information*

ABSTRACT: We report rapid photoinitiated intracomplex electron transfer (ET) within a "charge-disproportionated" myoglobin (Mb) dimer with greatly enhanced affinity. Two mutually supportive Brownian Dynamics (BD) interface redesign strategies, one a new "heme-filtering" approach, were employed to "break the symmetry" of a Mb homodimer by pairing Mb constructs with complementary highly positive and highly negative net surface charges, introduced through D/E → K and K → E mutations, respectively. BD simulations using a previously developed positive mutant, Mb(+6) = Mb(D44K/D60K/E85K), led to construction of the complementary negative mutant Mb(−6) = Mb(K45E, K63E, K95E). Simulations predict the pair will form a well-defined complex comprising a tight ensemble of conformations with nearly parallel hemes, at a metal−metal distance ∼18−19 Å. Upon expression and X-ray characterization of the partners, BD predictions were verified through ET photocycle measurements enabled by Zn-deuteroporphyrin substitution, forming the [ZnMb(−6), Fe³⁺Mb(+6)] complex. Triplet ET quenching shows charge disproportionation increases the binding constant by no less than ∼5 orders of magnitude relative to wild-type Mb values. All progress curves for charge separation (CS) and charge recombination (CR) are reproduced by a generalized kinetic model for the interprotein ET photocycle. The intracomplex ET rate constants for both CS and CR are increased by over 5 orders of magnitude, and their viscosity independence is indicative of true interprotein ET, rather than dynamic gating as seen in previous studies. The complex displays an unprecedented timecourse for CR of the CS intermediate **I**. After a laser flash, **I** forms through photoinduced CS, accumulates to a maximum concentration, then dies away through CR. However, before completely disappearing, **I** reappears *without another flash* and reaches a second maximum before disappearing completely.
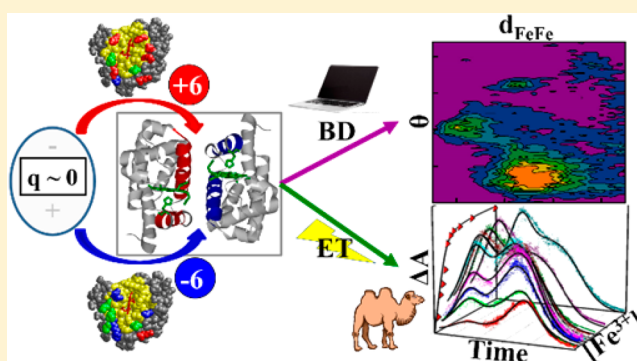
INTRODUCTION

Myoglobin (Mb), with a net charge near zero (wild-type horse heart Mb(WT), $q_{Mb} \sim -0.3e$), is a convenient "workbench" for probing the electrostatic control of binding and electron transfer (ET) between hemoprotein partners. Whether Mb(WT) is partnered with the highly negatively charged cytochrome b_5 (cyt b_5), the highly positively charged cytochrome c (Cc), or another nearly neutral Mb(WT), the partners react on a "dynamic docking" (DD) energy landscape (Figure 1) where binding is uncoupled from reactivity.[1−7] Protein partners on such a landscape exhibit multiple weakly bound configurations in rapid exchange between the complex and its unbound components, and reactive conformers are rare. In contrast, the limiting "simple docking" (SD) behavior has an energy landscape on which a complex exhibits one or a few well-defined reactive configurations that are in slow-exchange with their unbound partners. To shift DD-type complexes toward SD-type, we are exploring interface redesign strategies

that use Brownian Dynamics (BD) docking simulations to identify surface "hot-spot" residues where charge-exchange mutations would electrostatically enhance ET-active binding.[8−11]

The first application of this approach employed the negatively charged cyt b_5 as the target for binding Mbs with increasing positive charge. Three hot-spot residues on the heme face of the Mb surface (D44, D60 and E85) were identified where introduction of positive charges through D/E → K mutations were expected to enhance binding of cyt b_5 to Mb.[12,13] The success of this strategy was demonstrated by preparing Zn-deuteroporphyrin (ZnD) substituted Mb variants (ZnMb) involving combinations of the hot-spot residues, along with esterification of the porphyrin propionates. Photoinduced ET measured reactive binding,[14] and NMR chemical-shift
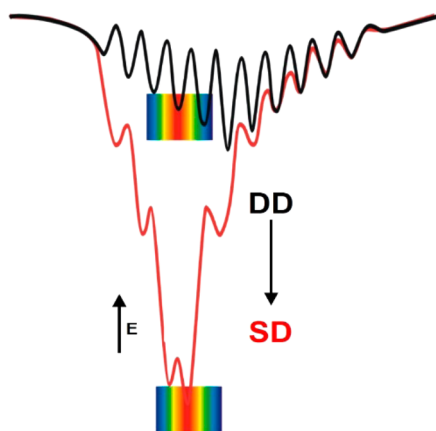
Figure 1. Dynamic docking (DD) and simple docking (SD) energy landscapes. ET reactive configurations represented by rainbow; ET-active geometries are red. Most stable geometries represented by wells.

perturbation mapping was used to structurally characterize the redesigned complex.[15,16] Increasing the positive charge near the Mb heme created a "reactive patch" defined as the area around the heme that contained the entire protein charge, and progressively transformed the weakly bound and poorly reactive DD-type [Mb(WT), cyt b_5] complex into a reactive complex whose enhanced affinity led to slow-exchange intracomplex ET on both the singlet and triplet time scales,[11] with the singlet rate approaching that for the initial step in photosynthetic charge separation.[14,17]

Here we extend these redesign efforts, and introduce a "charge-disproportionation" approach (Figure 2) for creating a
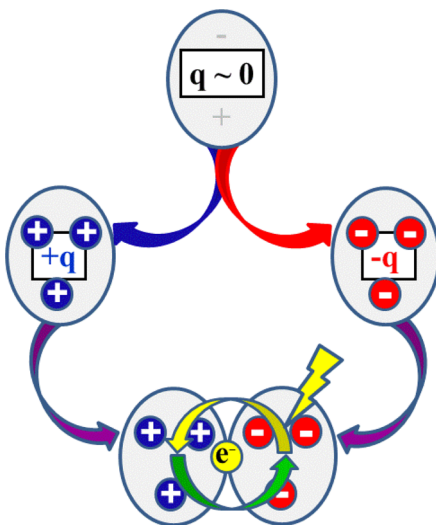

Figure 2. Myoglobin charge mutation dimerization strategy.

high-affinity Mb-Mb heterodimer that supports rapid intra-complex photoinduced ET. The strategy is to "break the symmetry" of a Mb homodimer by interacting a Mb construct having a highly positive surface charge with a complementary construct having a highly negative surface charge.

The previous redesign of the Mb surface to enhance interactions with cyt b_5 led to the preparation and character-ization of the positively charged Mb(D44K, D60K, E85K) triple mutant, Mb(+6): q = 5.9e, pH 7.[11,13,14] Using this Mb(+6) as the partner protein, we have now performed BD X

→ D/E surface mutant charge-reversal scans on Mb(WT) target protein to identify residues where addition of a negative charge to the Mb surface would most enhance docking with the Mb(+6). We then constructed and expressed a Mb(−6) triple mutant protein with X → D/E charge-reversal mutations at the three most favorable residues and prepared the Zn-substituted ZnMb(−6) variant, which enables study of the laser-flash induced ET photocyle for the [ZnMb(−6), Fe^{3+}Mb(+6)] complex. The simulations predict the [ZnMb(−6), Fe^{3+}Mb-(+6)] pair will form a well-defined, tightly bound complex that has a structure quite different from those of known globin dimers[18] and in particular Mb dimers;[19,20] triplet ET quenching titrations confirm this prediction.

Most dramatically, we observe an unprecedented progress curve for the charge-separated (CS) intermediate, **I**, formed by photoinitiated ET. In the numerous reports of an ET photocycle with photoinitiated charge separation (CS) followed by charge recombination (CR), in both covalently linked systems and noncovalent protein−protein complexes the timecourse for **I** has invariably been observed to exhibit a single maximum, in which **I** is formed through photoinitiated CS, reaches a maximum concentration, and then disappears through CR. Instead, the [ZnMb(−6), Fe^{3+}Mb(+6)] complex surprisingly exhibited a novel progress curve. As in all previous studies of photoinduced ET studies, photoinduced CS forms the intermediate **I**, which accumulates to a maximum concentration then begins to decay through CR. However, before completely disappearing, **I** reappears *without a second laser flash*, and the concentration climbs to a second, comparable maximum before finally disappearing completely through CR. These observations, in conjunction with a viscosity independence of the intracomplex ET rate constants, support the conclusion that the charge-disproportionation strategy has indeed generated a tightly bound, ET-active heterodimer well on the way to SD behavior (Figure 1).

■ MATERIALS AND METHODS

Brownian Dynamics Simulations. In the present study, negatively charged mutants of Mb(horse) (1YMB.pdb)[21] were designed using the BD docking protocol implemented in MacroDox, as previously described.[13,22] In the BD simulations, the "target" partner, here uniformly chosen to be Mb(WT) or a mutant that has been given a negative charge, is fixed in space and the Mb variant with three positively charged surface mutations (D44K, D60K, E85K) is allowed to undergo Brownian motion until it either "hits" the target or "wanders" outside the cutoff threshold distance (d = 200 Å). This is repeated for 10^4 randomly selected starting postions and the number of trajectories resulting in a hit are tallied. To maximize electrostatic attractions between partners, a Fe^{3+} ion is assumed for the positively charged Mb(+6), and a divalent metal ion (neutral porphyrin heme core) for the stationery target Mb. Ferrous-Mb is used as a surrogate for the ZnMb that is employed in photoinitiated ET measurements.

We performed two separate BD simulations (10^4 trajectories each) for docking ferri-Mb to the respective target ferro-Mb, each using a different criterion for determining whether a trajectory results in a hit. As in previous studies,[11−13,23] the two reaction criteria were as follows: (i) The distance between the centers of mass of the partners (COM criterion) which probes overall binding; a cutoff distance of 39 Å was used for the COM criterion. (ii) The distance between any one of the carboxylate oxygen atoms of a heme proprionate of ferro-Mb and a heme carboxylate oxygen atom of its ferri-Mb partner (criterion) to probe reactive binding. As the solvent exposure of the Mb heme is less than that of the b_5 heme, the cutoff distance for the O−O criterion was increased from the 4 Å used in the [Mb, cyt b_5] studies to 10 Å for the [ferro-Mb, ferri-Mb] simulations.

Protein Expression, Purification, and Characterization. The design, expression, and purification of Mb(WT) and the Mb(+6) triple mutant was previously reported, along with procedures for reconstitution of their apo forms with Zn-deuteroporphyrin (ZnD).[11] All Mb mutants were reconstituted with either Fe^{3+}-Protoporphyrin IX (Fe^{3+}) or ZnD as described previously.[11] Negatively charged proteins were isolated on and recovered from anion exchange (DEAE Seapharose Fast Flow resin, GE Healthcare) columns; positively charged proteins on cation exchange columns (CM Sepharose Fast Flow resin, GE Healthcare). All proteins were further purified using size exclusion chromatography (Sephadex G-25/G-50 medium resins, GE Healthcare). Reconstituted protein concentrations were measured using an Aglient 8453 UV−vis spectrophotometer; Soret maxima wavelengths and extinction coefficients were as follows: Fe^{3+}-Mb, 409 nm, $\varepsilon \sim 188$ M^{-1} cm^{-1};[24] ZnD-Mb, 414 nm, $\varepsilon \sim 361$ M^{-1} cm^{-1}.[2] All work with ZnD proteins was carried out in the dark to prevent photobleaching. Reconstituted proteins were flash frozen in liquid nitrogen, and stored at −80 °C in 10 mM KPi, pH 7.0 until used. Proper folding and stability of all mutants was validated by circular dichroism. Finally, all proteins' molecular weights and purity were verified by both mass spectrometry and SDS-PAGE analysis.

Crystallographic Structure Determination of Mb Variants. The light sensitivity of the proteins required carrying out crystallization procedures in the dark. All Mb crystals were obtained using the hanging drop vapor diffusion method with a 1:1 volume ratio of protein to reservoir solution at 20 °C. Crystals were soaked in cryoprotectant, mounted on loops, and flash frozen in liquid N_2. Native data sets were collected using synchrotron radiation at the Life Sciences Collaborative Access Team (LS-CAT) beamline (sector 21-ID-D) at the Advanced Photon Source, Argonne National Laboratory, using a Mar 300 CCD detector. The coordinates of the horse heart metMb structure (PDB ID 1YMB) were used for phasing by molecular replacement with the program Phaser.[25] Descriptions of the cofactors were obtained from the CCP4[26] monomer library or generated with the program JLigand[27] utilizing the appropriate library obtained from the grade Web Server. Ramachandran plots were calculated with PROCHECK[26,28] and validation was performed using both PHENIX[29] and SFCHECK.[30] Data collection and refinement statistics are shown in Table S3. Electron density maps were calculated using FFT[26,31] and figures were prepared using PyMOL.[32] The structures are described in SI and the atomic coordinates have been deposited in the PDB, Research Collaboratory for Structural Bioinformatics at Rutgers University: Fe^{3+}Mb(D44K/D60K/E85K) structure (PDB 4NS2); ZnMb (K45E/K63E/K96E) structure (PDB 4TWV); ZnMb(D44K/D60K/E85K) structure (PDB 4TWU); and Fe^{3+} Mb(K45E/K63E/K96E) structure (PDB 3RJ6).

Flash Photolysis Measurements. Cuvettes containing 2 mL of working buffer were stored open to the atmosphere in a N_2-filled glovebox overnight. Unless noted, all measurements were made in 5 mM potassium phosphate working buffer at pH 7. Stock solutions of protein were thawed on a cold block in the glovebox for several hours before the experiment. The concentration of the ZnMb in the final sample was 10 μM, as determined using $\varepsilon_{414} = 361$ mM^{-1} cm^{-1}.[2] The concentration of the ferri-quencher was varied from 5 to 120 μM for experiments with Mb(WT), and 2−50 μM for all other experiments, as determined spectrophotometrically (Agilent 8453 UV−vis) using $\varepsilon_{409}(Fe^{3+}Mb) = 188$ mM^{-1} cm^{-1}.[24]

Triplet quenching measurements were performed with an LKS.60 laser flash photolysis spectrometer (Applied Photophysics) fitted with a Xe lamp having pulsing capabilities and dual monochromators. Samples were excited with the output from a Nd:YAG Quanta-Ray INDI laser (Spectra-Physics), frequency-doubled to give excitation at 532 nm and an output power ~100 mJ. For slow triplet decays (<1000 s^{-1}), a setup modified from Applied Photophysics stopped-flow instrument was employed with a 9-stage photomultiplier tube for detection. Faster data collection was taken with an Agilent Infiniium 600 MHz digitizer and 5-stage photomultiplier tube for detection. The Xe lamp was pulsed to achieve the shortest time scales. Progress curves for the triplet decay were monitored at 475 nm; those for the ET

intermediate were collected at 559 nm. Typically, 10 shots were averaged on the slow time scale setup and at least 20 for the fast setup data collection. All kinetic experiments were performed at 20 °C.

■ RESULTS

We first describe a refined Brownian Dynamics design strategy intended to identify surface residues whose mutations will create Mb constructs with opposing high surface charges, which can then form a "charge-disproportionated" dimer that supports rapid intracomplex ET. The strategy is then implemented through the production of these highly charged Mb protein variants, and the results of ET kinetics and binding experiments are examined.

Interface Redesign. Our prior work indicated that in order to design a stable charge-disproportionated heterodimeric Mb complex that exhibits rapid ET, the two partners must have a large, negative charge product, $q_{Mb(+m)}q_{Mb(-n)}$, as would be the case for simple coulomb attraction between charged patches on the protein partners.[11] As the protein partners should have opposite charges, for simplicity, we employ the positive quantity,

$$qp = -(q_{Mb(+m)}q_{Mb(-n)})$$

Thus, larger values of qp correlate with complexes that exhibit greater electrostatic attraction, and in fact the previous study of [Mb, cyt b_5] ET complexes showed that the binding free energy increases linearly as a function of qp. The Mb variant with three positively charged surface mutations (D44K,D60K,E85K) yielded a [Mb(+6), cyt b_5] complex with $qp = 29$, as compared to $qp = -1.7$ for [Mb(WT), cyt b_5], which exhibited both remarkably enhanced binding and an equally dramatic increase in ET reactivity.[11−14]

This study, as in previous ones, begin with a BD interface design strategy that employed two criteria for classifying a trajectory as a "hit": the O−O criterion that probes reactivity, and the center-of-mass (COM) criterion that probes binding; the definitions of this study are defined in Materials and Methods. BD hit profiles resulting from simulations that dock the ferri-Mb(WT) to the ferro-Mb(WT) target with the COM criterion exhibit many hits distributed over the entire Mb surface, while the number of hits generated using the O−O criterion is negligible (Table 1), as expected from the

Table 1. Charge Products and Hit Counts for BD Simulations with Mb-Mb Dimers

$[Fe^{2+}, Fe^{3+}]$	qp	O−O (10 Å)	COM (39 Å)
Glu, Lys Mutations			
Mb(WT), Mb(−6)	−1.2	10	3532
Mb(WT), Mb(WT)	−0.06	55	3525
Mb(WT), Mb(+6)	1.5	25	3723
Mb(+6), Mb(−6)	24.6	3163	5097
Mb(−6), Mb(+6)	31.8	3311	5439

diminuitive charge product, $qp = -0.06$. The BD hit profiles for docking the ferri-Mb(+6) triple mutant to the ferro-Mb(WT) target protein are little improved (Figure 3, left). Despite the large positive charge on Mb(+6), qp remains small ($qp = +1.5$), so the COM hit profile for the [$Fe^{2+}Mb(WT)$, $Fe^{3+}Mb(+6)$] complex also shows hits distributed over the ferro-Mb(WT) surface, with very few reactive hits (O−O criterion) (Table 1).
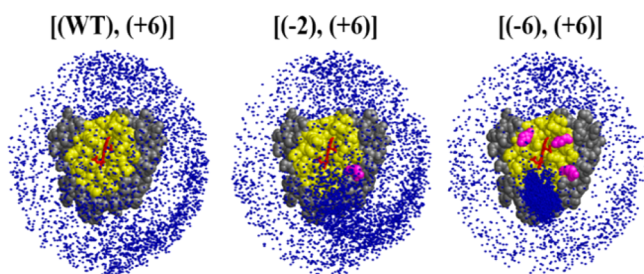
Figure 3. BD hit profiles for COM simulations where $Fe^{3+}Mb(+6)$ is docked onto different stationary $Fe^{2+}Mb$ targets. Mutations shown in magenta. Charge patch shown in yellow. Conditions: COM distance cutoff = 39 Å; 10 000 trajectories; outer boundary = 200 Å.

To identify "hot-spot" residues on the Mb(WT) surface that would create a negatively charged Mb mutant with increased affinity for and reactivity with Mb(+6), we carried out K/R/H → E charge reversal mutation scans on Mb(WT), changing each of the positively charged surface residues on Mb(WT) one-at-a-time into a negatively charged Glu residue.[33] The total number of COM hits is not significantly affected by any single surface mutation, but the number of hits using the O−O criterion varies with the mutation (Figure 4 upper), directly revealing hot-spot mutations for which the number of hits with the $Fe^{3+}Mb(+6)$ partner sharply increases. Three such residues (K45, K63 and K96) located near the heme (the "front" face)
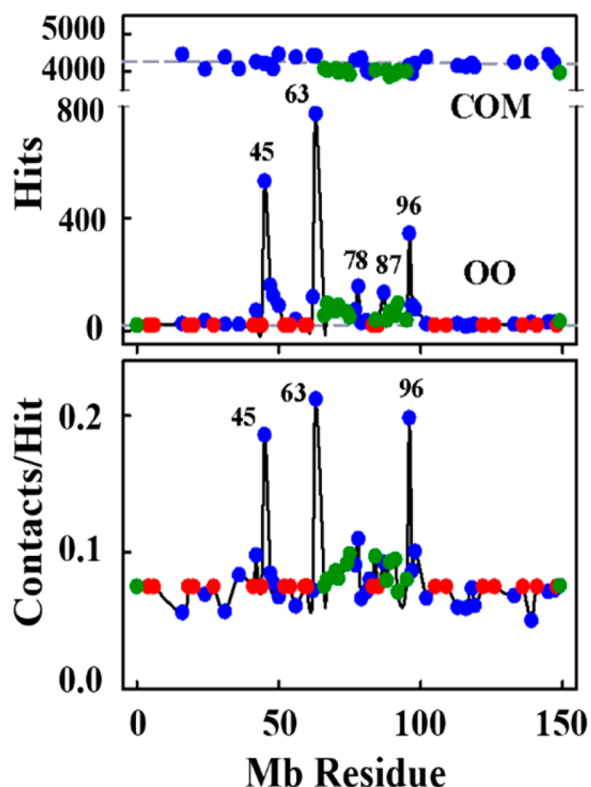

Figure 4. K/R/H → E charge reversal scans of $Fe^{3+}Mb(+6)$ docked to $Fe^{2+}Mb$ variants. (Upper) Number of hits as a function of residue number for K/R/H → E surface mutations in Mb(wt). COM (top line) and OO (bottom line) criteria. (Lower) Interface contacts between the heme of Mb(X) and a surface residue of Mb(+6) for the COM simulations in panel A, divided by the corresponding number of COM hits. Hotspot residues are labeled. Neutral residues (green), acidic residues (red), basic residues (blue).

result in a > 20-fold increase in the number of O−O hits. Two more residues (K78 and K87) are active to a lesser degree while mutations that change neutral residues along the "front face" E and F helices to Glu, corresponding to $\Delta q = +1$ (Figure 4, green symbols), did not significantly increase the number of O−O hits.

Although the hot-spot K → E mutations on Mb(WT) found using the O−O criterion are not apparent as an increased number of COM hits, an intriguing feature of the COM scan is that K → E mutations lead to partial clustering of the COM hits in the vicinity of the mutation, shown in Figure 3, center, for the mutation at residue 63 of Mb(WT). To assess the effectiveness of a mutation in achieving "reactive clustering", that is clustering in the vicinity of the heme, we further analyzed the interfaces of the hits from the COM simulations. With each charge-exchanged $Fe^{2+}Mb(WT)$ variant, we determined the total number of interface contacts between an atom of its heme with a surface residue on the $Fe^{3+}Mb(+6)$ partner, and determined the ratio of that number to the total number of hits in the simulation. This ratio is plotted in Figure 4, lower, which shows that the same three hot-spot residues found with the O−O criterion are also preeminent in enhancing interactions of the $Fe^{3+}Mb(+6)$ partner with the heme of $Fe^{2+}Mb(X)$. Examination of the corresponding contacts between the heme of $Fe^{3+}Mb(+6)$ and the surface of the mutants shows that the overwhelming number of hits associated with the clustering also involve the front face of the $Fe^{3+}Mb(+6)$; as a consequence of the large accumulation of positive charge on the $Fe^{3+}Mb(+6)$ front face, configurations where the backside of $Fe^{3+}Mb(+6)$ contacts the heme of Mb(X) are rare. Thus, this "heme-filtering" protocol successfully identifies "hot-spots" for enhancing reactive binding of $Fe^{3+}Mb(+6)$ with a charge-exchanged mutant.

The O−O criterion and heme-filtering protocol are not only mutually supportive, identifying the same three hot-spot residues for charge-exchange mutation, but indeed are complementary. The O−O criterion *requires* heme−heme contact as the criterion for binding. The heme-filtering strategy does not force this condition, rather, it is a natural outcome of the filtering protocol, thus showing that the mutations indeed generate face-to-face complexation. In addition, the heme-filtering approach requires just a single simulation (COM, which measures binding), and has the advantage of flexibility: hits can be filtered with respect to any selected location on the scanned protein, without having to rerun the simulation.

BD Simulations of [Mb(−6), Mb(+6)]. To computationally test whether combining the mutations at the three hot-spot locations would create a negatively charged Mb with enhanced binding to the reactive patch surrounding the heme edge of Mb(+6), we created the Mb(K45E, K63E, K96E) multimutant, Mb(−6), in silico. The COM BD hit profile for [$Fe^{2+}Mb(−6)$, $Fe^{3+}Mb(+6)$] (Figure 3, right) is strikingly different from that of the [$Fe^{2+}Mb(WT)$, $Fe^{3+}Mb(+6)$] reference complex (Figure 3 left): the COM hits for the moving $Fe^{3+}Mb(+6)$ on the fixed $Fe^{2+}Mb(WT)$ partner approximate to a uniform distribution on the $Fe^{2+}Mb(WT)$ surface, whereas the hits for the moving $Fe^{3+}Mb(+6)$, on the $Fe^{2+}Mb(−6)$ surface are highly localized in the heme vicinity (Figure 3, right).

The cluster of hits generated in the [$Fe^{2+}Mb(−6)$, $Fe^{3+}Mb(+6)$] COM simulation (Figure 3, right) corresponds to an ensemble of "heme−heme" configurations in which the heme edges roughly face one another across the interface, with a metal−metal distance ($d_{Fe−Fe}$) of ~21 Å or less. Examination

of the potential energy of protein−protein interaction for the hits shows that configurations in this cluster (∼60% of all COM hits) exhibit a strong electrostatic attraction between the partners. In contrast, the "halo" of hits outside this cluster (the remaining 40% of COM hits) involve protein configurations for which the electrostatic attraction is negligible, and where the reactive region of one or both partners is *not* located in the interface. These configurations thus contribute negligibly to both ET and to binding, and do not play a functional role.

To characterize the ensemble of functional configurations, we indexed each hit by its metal−metal distance ($d_{Fe−Fe}$) and heme−heme dihedral angle (θ), which we define in terms of the deviation from a reference structure where the heme of one partner is rotated by π relative to the other ("head-to-tail"), and generated a contour plot of the number of functional hits versus $d_{Fe−Fe}$ and θ (Figure 5). This plot shows a major population
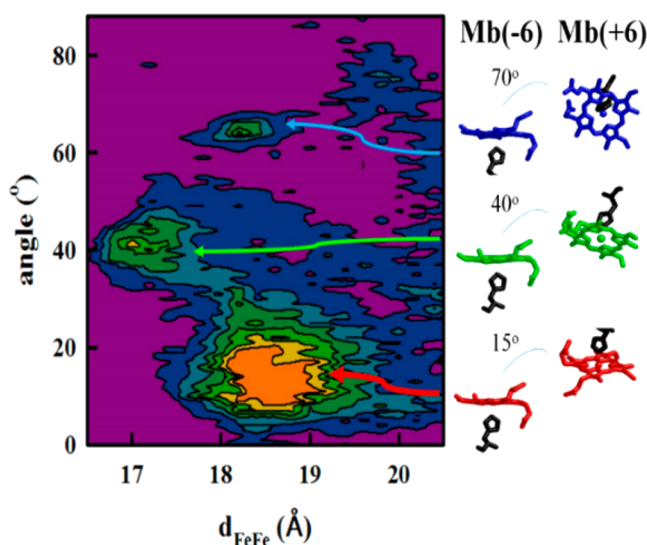

Figure 5. (Left) Contour plot of $d_{Fe−Fe}$ and θ for the reactive configurations (PE < −5 kcal/mol) from the hit profile for [$Fe^{2+}Mb(−6)$, $Fe^{3+}Mb(+6)$] (based on 10^5 trajectories) in Figure 3. This region includes 60% of the total hits. (Right) Representative geometries for the two hemes of the major peak with $d_{Fe−Fe}$ = 18−19 Å (red) and the minor peaks with $d_{Fe−Fe}$ = 17 Å (green) and $d_{Fe−Fe}$ = 18 Å (blue). Contour scale: orange >60 hits; yellow 48−60 hits; green 36−48 hits; cyan 24−36 hits; blue 12−24 hits; magenta <12 hits. Resolution: (0.2 Å; 1°); 10^5 trajectories.

centered around a heme−heme distance of ∼18−19 Å, and a heme−heme dihedral angle of $\theta \sim 15°$; the fit of a histogram of the angles for configurations in this population to a Gaussian distribution (Figure S1) gives a half-width of ∼6°. The plot also suggests there may be a minor population at $\theta \sim 40°$ and possibly a third one at ∼70°. The heme−heme orientations of representative configurations from the three clusters are shown along the right border of the contour plot (Figure 5, right). Notably, the secondary cluster at $\theta \sim 40°$ is centered at a slightly smaller metal−metal separation than the major form. This suggests that these minority configurations of the complex could potentially have higher ET rate constants.

We view this analysis as predicting that charge-disproportionation would convert the Mb-Mb homodimer from a weak DD pair to a well-defined [$Fe^{2+}Mb(−6)$, $Fe^{3+}Mb(+6)$] complex comprising an ensemble of tightly bound and highly reactive configurations in which the heme edges face one another, in a

nearly parallel geometry at an Fe−Fe distance ∼18.5 Å, including the possibility of a minority structure of even higher ET reactivity.

To characterize the predicted complex in greater detail, the residues involved in the ten closest contacts for *each* hit in the BD ensemble interface were identified and the total contacts for each residue of the two partners for all the configurations are plotted in Figure 6, left. The most frequently contacted residues
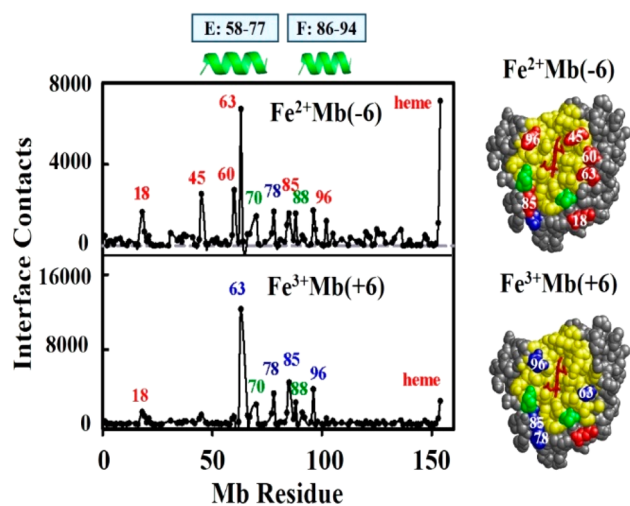

Figure 6. (Left) Number of interface contacts by residue for a COM simulation with $Fe^{2+}Mb(−6)$ and $Fe^{3+}Mb(+6)$. Coloring shows the top contacts on either side of the interface: red, acidic; blue, basic; green, neutral. The E and F helices are indicated by a ribbon above the top panel. (Right) Views of the surface of $Fe^{2+}Mb(−6)$ and $Fe^{3+}Mb(+6)$. Coloring of residues as on left; the reactive patches, which contain the heme edge and a charge equal to the net protein charge, is shown in yellow. Mbs are "head−tail" related by a rotation of π around normal to page ($\theta = 0$).

on each partner fall within oppositely charged "reactive patches" of the two proteins that contain the heme edge and a charge equal to the net protein charge as defined by the yellow regions in Figure 6, right.[11] These reactive patches include the surface atoms within 10 Å of a heme atom and involve residues from helices E (residues 58−77) and F (residues 86−94).

The five most frequently contacted residues on the $Fe^{2+}Mb(−6)$ side of the protein−protein interface all are negatively charged: D60, a heme propionate, and the three mutation sites (K45E, K63E and K96E). Less frequently, contact is made with three charged and two uncharged residues on the periphery of the interface: E18, T70, K78, and E85, P88. Correspondingly, the most-frequently interacting residues on the positively charged $Fe^{3+}Mb(+6)$ are the positively charged residues (K63, K78, K96, E85K), with less frequent interactions involving the heme and four uncharged residues (T70, A84, P88, Q91).

In short, analysis of the BD docking simulation indicates that the redesign strategy would produce a strongly binding, ET-active charge-disproportionated hetero-Mb dimer.

Structural Characterization and Verification of Mb Mutants. To implement the surface redesign strategy, we expressed, purified and reconstituted both the ferric-heme and ZnD forms of horse heart myoglobins (D44K, D60K, E85K) (FeMb(+6)) and (K45E, K63E, K96E) (FeMb(−6)). Three-dimensional structures obtained by X-ray crystallography

(Figures S2−S7, Tables S1−S3) confirm that none of the Mb variants (the two types of triple surface mutations as well as those with heme substitution by ZnD) show significant change from the WT protein structure. Substitution of heme by ZnD preserves the overall structure of the protein, but there are two deuteroporphyrin conformations in the X-ray structure of both triple mutants, a common occurrence in Mbs.[34,35]

Triplet Quenching Kinetics and Binding. To measure the binding and ET-reactivity of the charge-disproportionated partners we measured the ET photocycle introduced by ZnD substitution into the Mb(−6) partner. In the absence of ferri-Mb partner, the photoexcited triplet states of the Zn-substituted Mbs decay exponentially. The presence of a ferri-Mb partner quenches the ^{3}Zn-Mb excited state by electron transfer.

Figure 7 (upper) shows triplet decay traces for titrations by Fe^{3+}Mb(+6) of ZnMb(WT) (purple), and ZnMb(−6) (green). For the titration of ZnMb(WT), the charge product (qp) is small (qp ≃ 1.5, Table 2) despite the high positive charge on its partner. The decay curves remain exponential throughout the titration, and the decay constant, k_{obs}, increases linearly with the concentration of Fe^{3+}Mb partner (Figure 7, lower), implying the complex is in the fast exchange (FE) limit.[11,12] The slope of k_{obs} vs [Fe^{3+}Mb] gives the bimolecular quenching rate constant, which we take to equal the association rate constant, k_2 (Table 2).

In contrast, the pairs [ZnMb(−6), Fe^{3+}Mb(+6)] (Figure 7, green), and [ZnMb(+6), Fe^{3+}Mb(−6)] (data not shown) have charge-products qp = 31 and 25 respectively, and these triplet decay traces become biphasic during a titration, Figure 7. This indicates that the increased electrostatic interactions have shifted both complexes to the slow exchange (SE) regime. As is characteristic of this regime, the rate constant of the fast phase $k_{obs-fast} = k_D + k_q \sim k_q$ is nearly invariant with concentration (Figure 7, lower), and corresponds to that for intracomplex ET.

We note that switching the Zn substitution to the Mb(+6) partner eliminates the positive charge associated with the Fe^{3+}P, and decreases the negative charge on the Mb(−6) partner, yielding a decreased qp for the [ZnMb(+6), Fe^{3+}Mb(−6)] complex. As a result the intracomplex rate constant $k_{obs-fast}$ for the swapped pair [ZnMb(+6), Fe^{3+}Mb(−6)] pair is smaller than for its counterpart, [ZnMb(−6), Fe^{3+}Mb(+6)] and the small reduction in qp also causes a measurable reduction in bimolecular quenching constant, k_2, Figure 7, lower.

Heterodimer Affinity. Focusing on the [ZnMb(−6), Fe^{3+}Mb(+6)] complex, which has the larger value of qp, the complex is in SE and an *apparent* value for the binding constant, K_a', can be obtained by fitting the observed fraction of fast phase (bound complex), denoted F′, as a function of [Fe^{3+}Mb] to a simple binding isotherm (Figure 8, blue dash). However, whereas this analysis of the biexponential slow-exchange kinetics gives the correct values for the intra- and intercomplex ET rate constants, the binding constant K_a' must be corrected for quenching in the single state. This treatment of the progress curves assumes that *all* ZnMb photoexcited to the ^{1}ZnD excited state either return directly to the ground state or convert to the triplet state through intersystem crossing (ISC). However, we previously showed that singlet quenching within the preformed complex adds an additional decay channel for the ^{1}ZnMb, and this decreases the early time absorbance difference (A_0) of the [^{3}ZnMb(−6), Fe^{3+}Mb(+6)] relative to that of free ^{3}ZnMb(−6).[14,17] As a consequence, the actual fraction of bound ZnMb(−6), denoted F, is greater than the

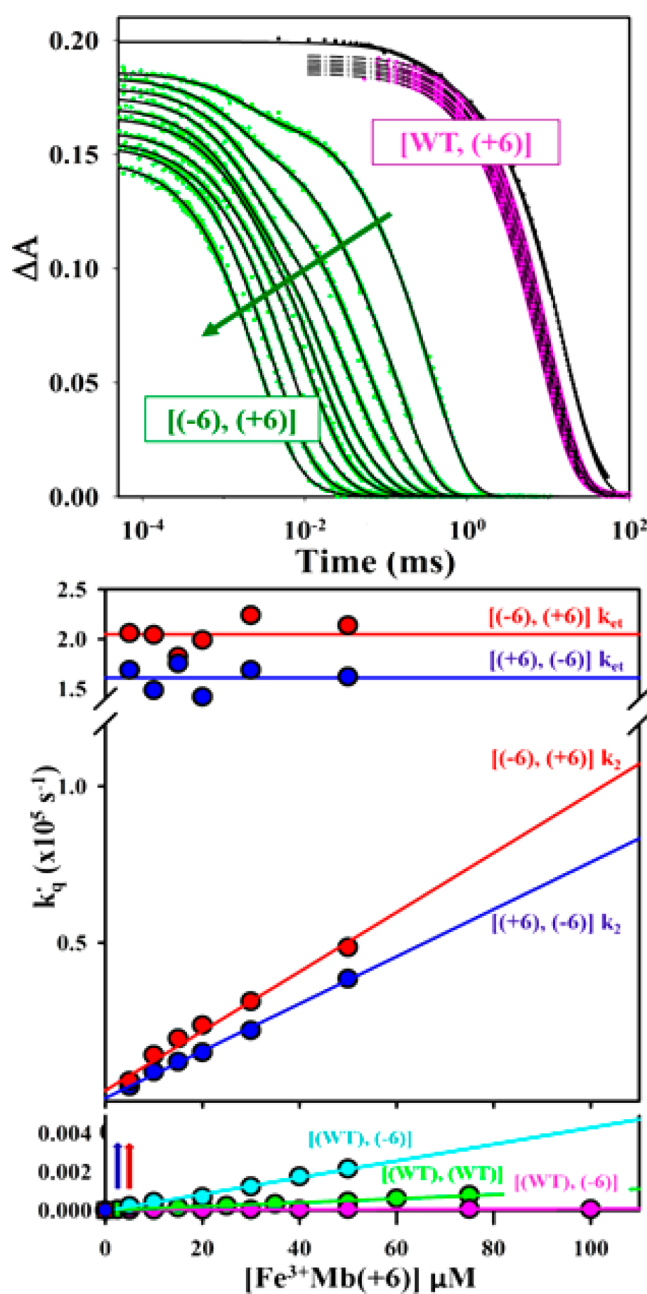**Figure 7.** (Upper) Triplet decay traces for titrations with [ZnDMb-(WT), Fe^{3+}Mb(+6)] (purple), and [ZnD(−6), Fe^{3+}Mb(+6)] (green). [Fe^{3+}Mb(+6)] = 0−120 μM purple, 0−50 μM green. (Lower) Fit parameters during [ZnDMb(X), Fe^{3+}Mb(X)] titrations. Data for the FE Mb(WT) (purple, green, cyan) complexes were analyzed with a single exponential decay function. Data for the SE [(+6), (−6)] (blue) and [(−6), (+6)] (red) complexes were analyzied with a biexponential decay function. Conditions: 10 μM Mb; 5 mM KPi, pH 7, 20 °C, 475 nm.

observed fraction, F′, and as a result, K_a' obtained from a simple fit of F′ underestimates the true binding constant, K_a.

The true K_a can, however, be obtained from the ^{3}ZnMb decay traces during a titration in two ways. The more direct is to correct the observed F′ for the effects of singlet quenching. The percent of ^{1}ZnMb that undergo ISC is given by φ, the ratio of the extrapolated zero-time triplet-ground absorbance difference at saturating concentrations of Fe^{3+}Mb, divided by free ZnMb absorbance difference. It is straightforward to show that

Table 2. Parameters Describing the Kinetics of Decay of Photoexcited ^{3}ZnMb

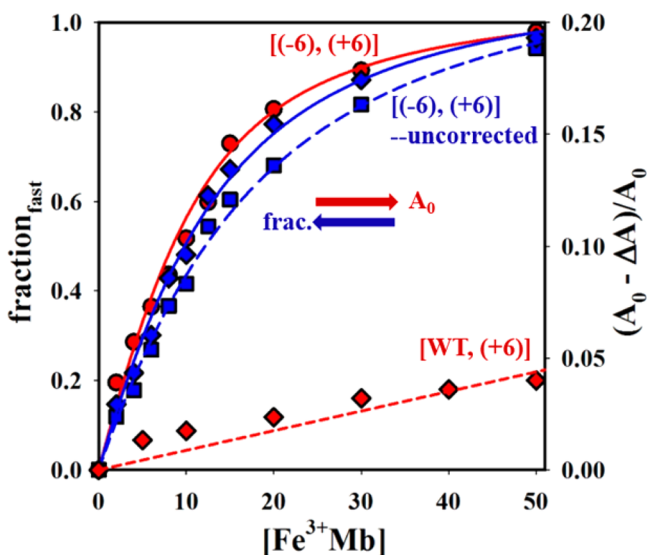|		kinetic parameter			
complex	qp	regime	k_2 (M^{-1} s^{-1})	K_a (M^{-1})	k_{et} (s^{-1})
ZnMb(WT)/Fe^{3+}Mb(−6)	−1.2	FE	1.0×10^5	<5	−
ZnMb(WT)/Fe^{3+}Mb(WT)	−0.06	FE	1.0×10^6	<5	−
ZnMb(WT)/Fe^{3+}Mb(+6)	1.5	FE	4.2×10^6	<5	−
ZnMb(+6)/Fe^{3+}Mb(−6)	25	SE	1.0×10^9	4.0×10^4	$1.5(2) \times 10^5$
ZnMb(−6)/Fe^{3+}Mb(+6)	31	SE	$5(1) \times 10^9$	$1.0(2) \times 10^5$	$2.0(2) \times 10^5$
ZnMb(+6)/Fe$^{3+}b_5$	29	SE	$4(2) \times 10^9$	$9(1) \times 10^4$	2.0×10^5
Hb [α_1(Zn), β_2(Fe)]		SE	−	−	18

Figure 8. Binding curves derived from [ZnDMb(−6), Fe^{3+}Mb(+6)] titration. Data for early time absorbance drop A_0 [(−6), (+6)] (red circles, solid), A_0 [(WT), (+6)] (red diamonds, dashed), [(−6), (+6)] fast phase fraction (blue squares, dashed), and [(−6), (+6)] fraction fast corrected for singlet activity (blue diamonds, solid) were all fit to a 1:1 binding isotherm. Note: [(WT), (+6)] data extends to 120 μM, not shown.

at each point in a titration, F, the actual fraction of bound complexes, is related to F′ through φ as follows,

$$\varphi = \frac{\Delta A^\infty}{\Delta A^{free}} \qquad F = \frac{F'}{\varphi + F'(1 - \varphi)} \qquad (1)$$

The corrected fractions of bound complex, F, as obtained by applying eq 1 to the observed fractions F′, are also plotted in Figure 8 (blue line); their fit to a binding isotherm yields $K_a = 1.1 \times 10^5$ M^{-1}.

The second method of determining K_a is to use the progressive decrease in zero-time triplet-ground absorbance as a function of Fe^{3+}Mb concentration, $\Delta A^{[Fe]}$. At any given point in a titration, F is given by,

$$F = \frac{\Delta A^{free} - \Delta A^{[Fe]}}{\Delta A^{free}}$$

A fit of F determined in this way to a binding isotherm yields $K_a = 1.2 \times 10^5$ M^{-1}, the same value within error, as obtained by the use of eq 1 to calulate Fs from the F′ obtained from the decomposition of the triplet decay traces. The resultant K_a for selected Mb complexes are given in Table 2; that for [ZnMb(−6), Fe^{3+}Mb(+6)] is no less than ∼5 orders of magnitude greater than that for Mb(WT) complexes.

Kinetics and Binding of the Charge Separated Intermediate, I. The optical spectra of the ZnMb variants (Figure S8) are identical, as are the ^{3}ZnMb−ZnMb difference spectra. Thus, the charge-separated intermediates that form upon excitation of all the [ZnMb, Fe^{3+}Mb] complexes, I = [D$^+$A$^-$], could be followed equally by monitoring the transient absorbance changes at the ^{3}ZnMb−ZnMb isosbestic point, 559 nm.

In all previous studies of photoinitiated ET between noncovalent protein partners the absorbance difference associated with a charge-separated intermediate I rose to a maximum then decayed, regardless of whether the curves were mono- or multiphasic. In the case of related [Mb, b_5] complexes, the maximum accumulation of I decreased dramatically as charge product (qp) increased, because the rate of formation of I increased more slowly than the rate of charge recombination, decreasing the extent to which I accumulated.[36]

The complexes of ZnMb(WT) with Fe^{3+}Mb(WT) and Fe^{3+}Mb(+6) partners (qp < 1.5) likewise show a single maximum in the progress curves for I, in Figure 9 (purple, green). However, in contrast to [Mb, b_5] complexes, the additional increase in qp for [ZnMb(−6), Fe^{3+}Mb(+6)] (qp ∼ 31) causes an increase in the maximum accumulation of I. Most dramatically, and completely without precedent, the time-evolution of I for [ZnMb(−6), Fe^{3+}Mb(+6)] exhibits two
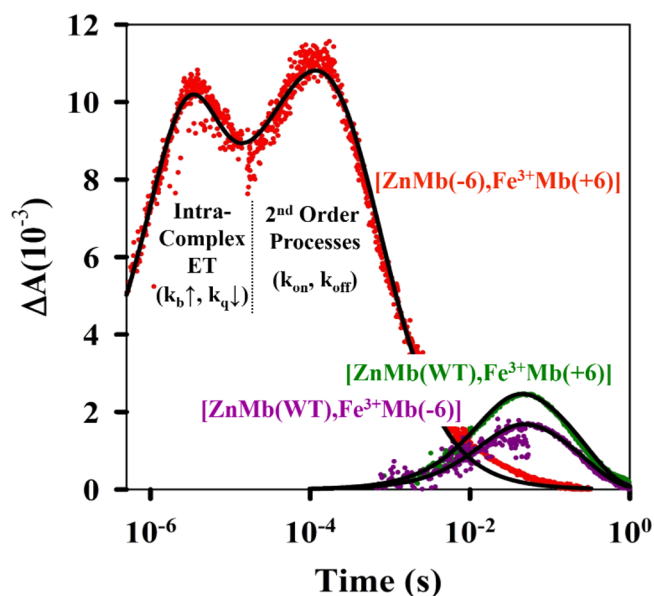

Figure 9. Progress curves for the charge separated intermediate I, for [ZnDMb(X), Fe^{3+}Mb(X)]. [(WT), (−6)] (purple), [(WT), (+6)] (green), [(−6), (+6)] (red).

distinct phases, each with its own maximum (Figure 9, red). Figure 10 shows two perspectives for the changes in the
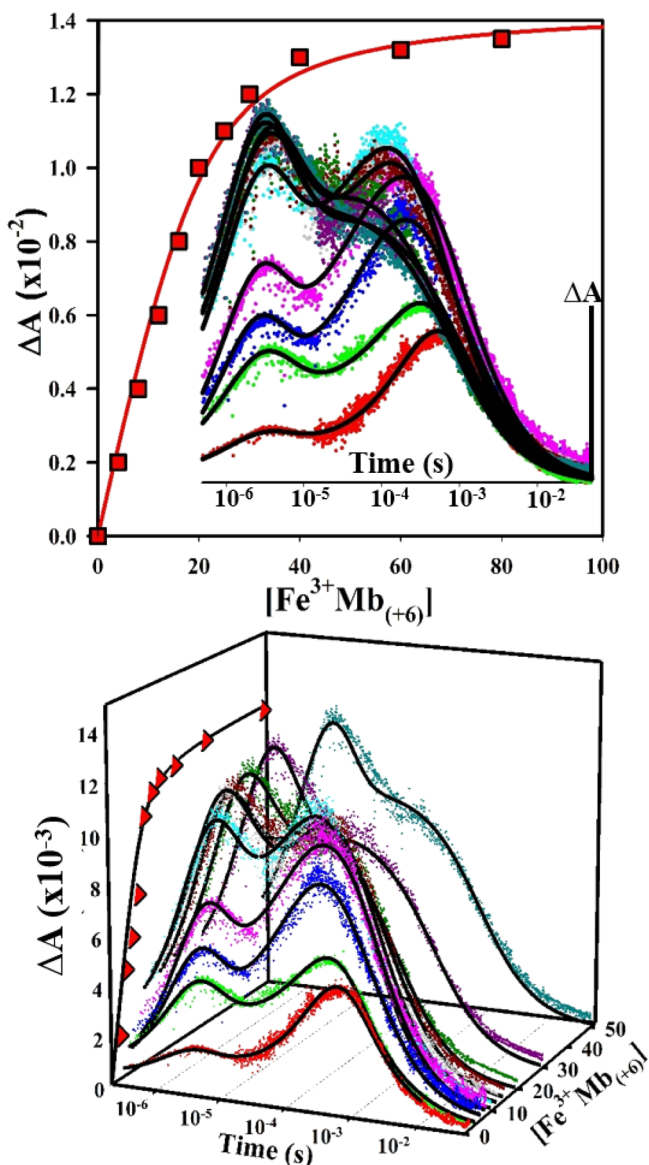

Figure 10. (Upper) Progress curves for **I** for [ZnDMb(−6), $Fe^{3+}Mb(+6)$] throught a titration (red, 2 μM Fe3+Mb(+6), green 4 μM, blue 6 μM, pink 8 μM, cyan 10 μM, dark red 12.5 μM, dark yellow 15 μM, dark green 20 μM, dark pink 30 μM, dark cyan 50 μM). Maximum ΔA values for the fast phase were fit to a 1:1 binding isotherm (red squares upper/red triangles lower, red line), binding constant, $K_a = 1.2 \times 10^5$ M^{-1}. (Lower) 3D rendering of **I** progress curves. Conditions: 10 μM ZnDMb(−6), 5 mM KPi, pH 7, 20 °C.

progress curves of the charge-separated intermediate **I** during a titration of ZnMb(−6) with $Fe^{3+}Mb(+6)$; the upper panel of Figure 10 clearly shows the two temporal evolution of the maxima during the course of a titration, while the lower panel more clearly shows how the amplitudes evolve.

Figure 10 also contains a plot of the absorption-difference maximum for the **I** fast phase as a function of [$Fe^{3+}Mb(+6)$]: as [$Fe^{3+}Mb(+6)$] increases during the titration, the early time "fast" phase accumulates to saturation, as expected for a simple binding isotherm. This shows that this early time phase corresponds to cyclic ET within the preformed 1:1 complex in

slow exchange. At all points in the titration, the maximum absorbance difference of the fast phase of the **I** progress curve occurs at $\tau_1 \sim 5$ μs, as this phase appears and disappears with constant rise and fall times governed by intracomplex ET rate constants.

The slow **I** phase exhibits a second, later-time, absorbance maximum, which appears without a second laser flash. This phase has an exponential rise with the bimolecular triplet-state quenching rate, $k_2 \sim [Fe^{3+}Mb(+6)]$. As a result, the absorbance maximum for this phase shifts to shorter times during a titration. Its amplitude initially increases as the quencher concentration increases, then decreases as the amount of free ZnMb(−6) decreases (Figure 10).

The fall of the slow phase of **I** is not exponential. Rather, the progress curves exhibit a "tail" indicative of a second order process after 1 equiv of $Fe^{3+}Mb(+6)$ has been added, as shown by the linear dependence of the reciprocal of the absorbance difference upon time at long times (Figure S9). This process is even present at ratios less than 1:1 ZnMb(−6): $Fe^{3+}Mb(+6)$, but is hard to recognize because **I** must accumulate sufficiently to accurately visualize this effect. This implies **I** must in part dissociate to free ZnD$^+$Mb(−6) and $Fe^{2+}Mb(+6)$ after ET, with the long-time behavior determined by their rebinding with charge recombination.

Overall, a description of the slow phase recovery of the ground state therefore must incorporate dissociation of **I** in competition with CR, recombination of the dissociated components of **I**, as well as association and reaction of free ^{3}ZnMb(−6) with $Fe^{3+}Mb(+6)$. As a complicating feature, the dissociated ZnD$^+$Mb(−6) is free to bind with excess $Fe^{3+}Mb$-(+6), preventing reaction with the liberated $Fe^{2+}Mb(+6)$. Thus, the $Fe^{3+}Mb(+6)$ free acts as an inhibitor of charge recombination.

This interpretation of the two phases as intracomplex (early time phase) and second-order (later-time phase) is confirmed by effects of changing viscosity on the triplet quenching decay curves and the timecourse of **I** for the [ZnMb(−6), $Fe^{3+}Mb(+6)$] complex. Figure 11 shows the response of these curves in an experiment with a fixed ratio of $Fe^{3+}Mb(+6)$/ZnMb(−6) = 1. In both the progress curves for triplet-decay and **I**, the fast phase is invariant with increasing η, which confirms that these phases are associated with the
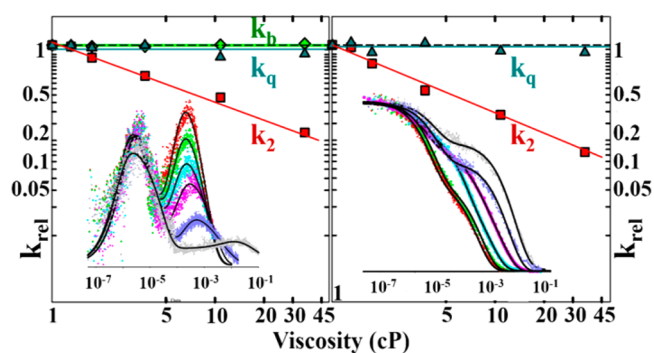

Figure 11. Viscosity dependence of timecourses for **I** (left) and triplet quenching curves (right) for 1:1 ZnDMb(−6)/$Fe^{3+}Mb(+6)$. Viscosity indicated by color on the insets: 1.0 cP (red), 1.3 cP (green), 1.8 cP (cyan), 3.7 cP (pink), 10.8 cP (blue), 35.5 cP (gray). All rates normalized to values presented in Table 3. Quenching (k_q) is represented by triangles, back rates (k_b) by diamonds, and association rates (k_{on}) by squares.

intracomplex photocycle, ET quenching to yield **I**, followed by charge recombination within **I**, and that neither process is modulated by intracomplex dynamic processes.

In contrast, the slow phases of ET quenching and timecourses of **I** are strongly modulated by changes in viscosity, as expected for bimolecular quenching of unbound ^{3}ZnMb(-6) and recombination of the dissociated partners of **I**. In particular, the second maximum in the progress curve of **I** shifts to longer time as the second-order rate constants slow, and decreases in amplitude as the triplet ET quenching decreases.

[Mb, Mb] Kinetic Scheme. *Description of Kinetic Scheme.* The behavior of the progress curves for **I** of the [ZnMb(-6), Fe^{3+}Mb($+6$)] ([D, A]) complex during a titration indicate that a complete kinetic description of the ET photocycle displayed by the ($+6$)/(-6) Mb pair must incorporate the features presented in Scheme 1. The scheme

Scheme 1
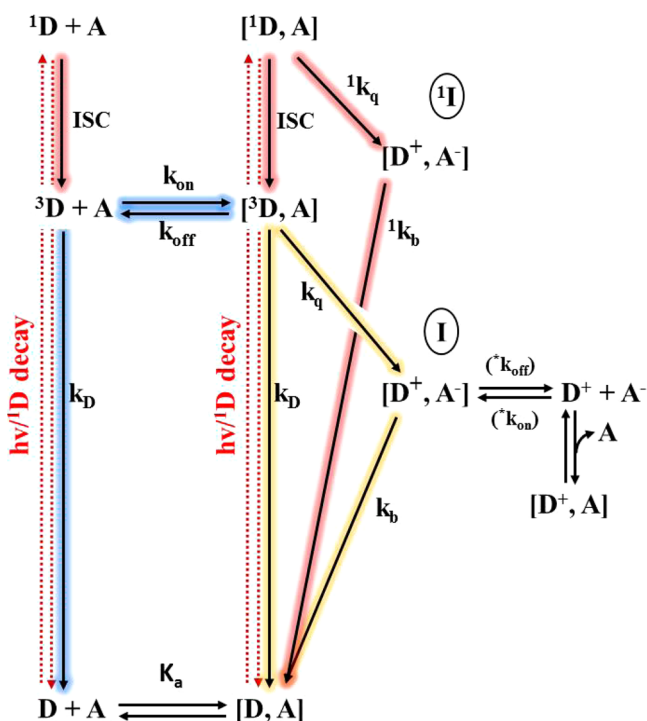
begins with a pre-equilibrium between bound and free ZnMb(-6) (D) and Fe^{3+}Mb($+6$) (A) (K_a as determined above), with the equilibrium reflecting formation and dissociation rate constants, (k_{on}, k_{off}) that are taken to describe both the ground and excited states. Free and bound ZnMb(-6) are photoexcited equally to ^{1}ZnMb(-6) (^{1}D). Photoexcitation of bound complex yields the singlet state complex [^{1}ZnMb(-6), Fe^{3+}Mb($+6$)] ([^{1}D, A]), which can undergo decay to ground, singlet ET to form ^{1}**I** (^1k_q), or intersystem crossing to the triplet state complex [^{3}ZnMb(-6), Fe^{3+}Mb($+6$)] ([^{3}D, A]). Conformations of the complex that can undergo such rapid ET form a charge-separated complex that returns to ground promptly (^1k_b), hence on the triplet time scale this rapid photocycle merely appears as a singlet decay process that diminishes the early time triplet-ground absorbance A_0, as discussed above. Indeed, all photoinitiated processes involving ^{1}D and [^{1}D, A] are so rapid compared to formation and dissociation of the complex that these latter processes are not included for the singlet state in Scheme 1.

The photogenerated triplet-state ^{3}ZnMb(-6) in a preformed complex can decay to ground (k_D) or undergo ET to form **I** = [Zn$^+$Mb(-6), Fe^{2+}Mb($+6$)] ([D$^+$, A$^-$], k_q); once **I** is formed, it can undergo CR to regenerate the ground complex (k_b) or dissociate into its charge separated components, Zn$^+$Mb(-6) and Fe^{2+}Mb($+6$) (D$^+$ + A$^-$), with rate constants *k_{on}, and *k_{off}. Once dissociation has occurred, it is possible for excess Fe^{3+}Mb($+6$) to bind the free Zn$^+$Mb(-6) to form an "inhibited" complex ([D$^+$, A]), preventing recombination and creating an inhibitive effect.

In parallel with the transformations of the preformed complex, photoexcited free ^{1}ZnMb(-6) rapidly undergoes ISC to ^{3}ZnMb(-6) in competition with decay to ground. Free ^{3}ZnMb(-6) can decay to ground (k_D) or bind an Fe^{3+}Mb($+6$) (second-order rate constant, k_{on}) to generate a photoexcited complex that undergoes the three processes described above.

The Kinetic Scheme and Progress Curves for I. The progress curves for **I** collected during a Fe^{3+}Mb($+6$) titration of ZnMb(-6) (Figure 10) have been fit to Scheme 1 through numerical integration of the differential rate equations implied by the scheme. Two approaches were investigated; all curves were fit individually, and the set of curves was fit globally. The two approaches yield the same values for the kinetic parameters k_q, k_b, k_{on}, and k_{off} (Table 3).

Table 3. [ZnMb(-6), Fe3+Mb($+6$)]: ET Rate Constants from Fit to Scheme 1

k_q (s^{-1})	k_b (s^{-1})	k_{on} (M^{-1} s^{-1})	k_{off} (s^{-1})
$1.3(2) \times 10^5$	$8.0(5) \times 10^5$	$5.0(5) \times 10^9$	$4(1) \times 10^4$

Intracomplex Photocycle, Fast Phase. Approximately three-quarters of the preformed triplet-state complexes undergo photoinduced ET to generate the CS intermediate **I**, the rest dissociating before ET can occur: the fraction of triplet states that undergo ET is $\varphi_{ET} = \frac{k_q}{k_{off} + k_q} \sim 75\%$. The appearance of **I** in the intracomplex fast phase of its progress curve is faster than the decay of the triplet state in the bound complex (triplet fast phase) in every stage of the titration, indicating that this rate is in fact the rate of ET return to the ground state, $k_b > k_q$, a relationship rarely considered. Once formed, **I** can either undergo CR to complete the intracomplex photocycle with rate constant k_b, or dissociate. Almost all **I** completes the intracomplex ET photocycle; according to Scheme 1, the fraction of **I** that dissociates is only $F_{disc} = \frac{k_{off}}{k_{off} + k_b} \sim 2.5\%$.

Second-Order, Slow Phase. The fits to Scheme 1 further capture the systematic increase in the rate of appearance of the slow phase of the **I** progress curve with increasing [Fe^{3+}Mb($+6$)], which corresponds to the triplet bimolecular quenching constant of free ^{3}ZnMb(-6) by Fe^{3+}Mb($+6$). The amplitude and decay of the slow phase is governed by second order dissociation/association of the CS intermediate **I**. In principle, the rate constants for dissociation/association of **I** should differ from those for the ground/excited-state complexes, as the ET process lowers the positive charge on the Mb($+6$) partner, and increases the positive charge on the Mb(-6) partner. This has been accounted for in Scheme 1 (*k_{on}, *k_{off}) but in fact any differences are negligible. Note that even at very high [Fe^{3+}Mb($+6$)] concentrations, where the fraction of bound ZnMb(-6) approaches unity, the dissociation and subsequent rebinding yields a small second order contribution to charge

recombination that dominates the long-time behavior of the **I** progress curves (Figure S9).

Lastly, free $Fe^{3+}Mb(+6)$ can bind to $Zn^{+}Mb(-6)$ released by dissociation of **I**, and by sequestering the $Zn^{+}Mb(-6)$ thus "inhibit" the second order recombination of $Zn^{+}Mb(-6)$ and $Fe^{2+}Mb(+6)$ and the charge recombination. As seen in Figure S9, the return to ground indeed slows as $[Fe^{3+}Mb(+6)]$ is increased, but the effect is small.

Finally, the fits to the **I** progress curves provide an additional method of calculating the binding affinity for the charge-disproportionated complex: $K_a = k_{on}/k_{off} = 1.25 \times 10^5$ M^{-1} in agreement with the two methods associated with triplet quenching (Table 2); the three methods yield a consensus best-value binding constant, $K_a = 1.0(2) \times 10^5$ M^{-1}.[37]

Viscosity. To test which of the rate constants were controlled by "gating" motions, progress curves for **I** were collected for samples at fixed ratio, $[ZnMb(-6)]/[Fe^{3+}Mb(+6)] = 1$, but prepared with a range of viscosity, η, and were collected and fit (individually and globally) to Scheme 1, allowing for an inverse dependence on η: $k_i(\eta) = k_i^0 \ \eta^{-1}$. Visual inspection of the viscosity-dependent traces suggests that the rate constants for intramolecular CS and CR, k_q and k_b, are independent of η, and this was confirmed by the global fitting procedure. The rate constants for complex formation and dissociation, k_{on}, k_{off} and $*k_{on}$, $*k_{off}$ (data not shown) in contrast decrease with increasing viscosity, as expected. For example, Figure 11 shows that the bimolecular quenching k_{on} decreases in this fashion. The k_i^0 for the viscosity-dependent processes are given in Table 3.

■ DISCUSSION

In this report, we have employed a refined BD interface redesign strategy to create a "charge-disproportionated" $[Mb(+6), Mb(-6)]$ complex in which three $K \rightarrow E$ charge reversal mutations on the Mb(WT) surface generate a Mb(−6) mutant that binds to the positively charged Mb(+6) triple mutant. These constructs were then successfully expressed, characterized and crystallized, and subjected to photoinitiated ET measurements. The ET experiments validate the expectation based on the BD simulations, that the resulting hetero-Mb dimer would form a well-defined, tight-binding complex that exhibits high ET activity. As a surprising "bonus", the CS intermediate, **I**, formed within this complex shows an unpredented timecourse—accumulating to a maximum concentration, disappearing, then reappearing to a second maximum before finally vanishing.

Brownian Dynamics Interface Design Strategy. Redesigning the interface of the nearly neutral Mb to create complementary Mb(+m), Mb(−n) "charge-disproportionation" partners represents a different kind of challenge than redesigning the interface of either the Mb-b_5 or Mb-Cc pairs, where the b_5 and Cc partner proteins are already highly charged. It is not obvious how to simultaneously introduce paired charges on a neutral protein to create partner proteins, with paired negative and positive residues, so as to optimize binding and reactivity between the two constructs. However, as we had already designed and expressed a Mb(+6) variant to interact with a negatively charged protein, b_5, BD simulations/scans were conducted using this positively charged Mb as a template against which to introduce negative charges onto the surface of a neutral Mb.

An implicit assumption inherent to the BD strategy is that ET rate constants for members of an ensemble of structures vary with the heme−heme separation, orientation and/or ET

pathways,[22] and thus generation of a complex with enhanced ET would involve enhancement of "face−face" contacts between the heme edges. Our previously described "O−O" criterion for identifying "hot-spots" for surface charge-exchange mutations has been augmented by a new, refined "heme-filtering" design procedure, the two together enabling us to generate complementary noncovalent $[Mb(-n), Mb(+6)]$ dimers with high homology and heme-facing-heme structures. BD simulations with both procedures led to the identification of a trio of surface hot-spot residues where introduction of negative surface charges through $X \rightarrow D/E$ mutations were predicted to cause a large proportion of BD hits by the Mb(+6) on a mutant that satisfies both the COM binding and heme−heme reactivity filter criteria (Figure 4). Notably, the O−O criterion and heme-filtering protocol are not only mutually supportive, but indeed are complementary. The O−O criterion *requires* heme−heme contact for a BD hit. The heme filter strategy does not force this condition; rather, it is a natural outcome of the filtering protocol, thus showing that the mutations indeed generate face−face complexation.

The most significant single-residue changes were associated with the Mb front face (+ → −) charge reversal mutations of residues K45, K63, and K96, which led us to introduce the K45E/K63E/K96E triplet of charge-reversal mutations, resulting in the Mb(+6) construct studied here.[38] BD simulations in which this $Fe^{3+}Mb(+6)$ was docked to the stationary $Fe^{2+}Mb(-6)$ showed that the "functional" BD hits, those that contribute to binding and ET, are sharply focused near the heme on the Mb(−6) front face (Figure 3). Inspection of the structures associated with these hits showed a large increase in the number of contacts between residues in the "charged patches" that surround the heme (Figure 4). Each of these functional configurations was indexed by its metal−metal distance (d_{Fe-Fe}) and heme−heme dihedral angle (θ), which allowed the generation of a contour plot of the number of functional hits versus d_{Fe-Fe} and θ, Figure 5. This graphically shows that the hits are tightly clustered, and represent the creation of a well-defined complex comprising an ensemble of highly similar structures where the heme edges of the partners face one another at an Fe−Fe distance of ∼18−19 Å, with nearly parallel heme planes.

Considering the absence of a defined structure for the parent, weakly interacting $[Mb(WT), Mb(WT)]$ homodimer, or the weakly interacting $[Mb(WT), Mb(+6)]$ heterodimer (Figure 3), the conversion to such a tight ensemble of structures through only three well-placed surface mutations (96% homology between partners), is remarkable. For completeness, we note Figure 5 suggests a possible second (or even third) minority conformation. As discussed in the next subsection, measurements of the ET photocycle for the $[ZnMb(-6), Fe^{3+}Mb(+6)]$ heterodimer showed tight binding and high ET reactivity, as predicted by the BD simultations.

ET Photocycle. Measurements of the ET quenching of the triplet state show that (*i*) the binding constant for the complex has been increased by *no less than* ∼ 5 orders of magnitude through charge disproportion, and (*ii*) the rate constants for both steps in the intracomplex ET photocycle are 4 orders of magnitude greater than those for the well-defined reference "complex" between the α_1 and β_2 subunits within the mixed-metal Hb hybrid tetramer.[39,40] (Table 2), where the hemes are *not* edge−edge.

To describe the complete ET photocycle, we employed Scheme 1. Using numerical integration of the analogous rate

equations, progress curves for **I** were fit to Scheme 1, yielding the rate constants for charge separation (k_q), charge recombination (k_b), complex association (k_{on}), and complex dissociation (k_{off}). Note that the rate of charge recombination, k_b, is larger than that of charge separation, (k_q), as seen in our studies of intracomplex ET in Hb,[39,40] for example, but nevertheless a kinetic phenomenon not frequently encountered in studies of protein−protein ET.

Surprisingly, the [ZnMb(−6), Fe^{3+}Mb(+6)] progress curve for charge recombination of the CS intermediate, **I**, formed by photoinitiated Zn* → Fe^{3+} ET shows a completely unprecedented shape. Photoinduced charge separation produces the intermediate **I**, which accumulates to a maximum concentration, then dies away through charge recombination as seen in all previous studies of photoinduced ET. However, before completely disappearing, **I** reappears *without a second laser flash* - its concentration climbs to a second maximum before it finally disappears, to generate a timecourse for **I** with two well-resolved maxima (Figures 9, 10), here denoted a "2H" type curve. To our knowledge, all prior studies of non-covalently linked small-molecule photo-donor/acceptor pairs and inter-protein ET partners have shown progress curves for **I** exhibiting only one maxima, denoted here "1H" curves.[41] This includes partners with binding affinities at both ends of the broadest range of values, $10^0 \rightarrow 10^9$ M^{-1}. For example, the tightly bound α_1/β_2 complex of mixed-metal hemoglobin (Hb) hybrids[40,42] exhibits only intracomplex ET, and its intermediate exhibits a simple *1H* progress curve with a single maximum, characterized by the appearance of the intermediate with the intracomplex CR rate constant and its disappearance with the rate constant for triplet decay, as expected for the ET photocycle of a simple docked complex. In the other extreme, intermediates for the very weakly bound [Mb(WT), b_5][43] complex *also* exhibit a 1H curve.

The kinetic behavior of the photoexcited triplet and the unusual timecourse for the ET intermediate have been fully described by Scheme 1, as illustrated in Figure 10. In fact, Scheme 1 provides a unified kinetic scheme for ET in protein−protein complexes, and can describe the full range of behaviors seen for interprotein ET photocycles. The behavior of the scheme is determined by three critical parameters: k_q, k_b, and K_a. One can visualize the properties of the scheme by fixing the ET rate constants k_q and k_b, and varying K_a; for concreteness we choose the ET rate constants associated with [ZnMb(−6), Fe^{3+}Mb(+6)] complexes (Table 3; $k_q \sim 1 \times 10^5$ s^{-1}, $k_b \sim 8 \times 10^5$ s^{-1}). As we further take complex association to be diffusion limited ($k_{on} \sim 10^9$ M^{-1} s^{-1}), variation in K_a can also be viewed in terms of variations in the dissociation rate constant, k_{off}. We furthermore focus on the most illuminating solution conditions, a 1:1 ratio of the ET partners, taking each at 10 μM as for the 1:1 trace in the titration ZnMb(−6) by Fe^{3+}Mb(+6).

Simulations calculated using Scheme 1 under the above specified conditions as K_a varies by 10 orders of magnitude are shown in Figure 12, upper. The behavior of the scheme can be discussed in terms of three ranges for K_a.

(i) When $K_a > 10^6$ M^{-1}, the progress curves for **I** exhibit only a single phase (*1H*) at early times ($t \lesssim 10^{-4}$ s). In this range, complexes are tightly bound, and only intracomplex ET is observed. From both the point of view of triplet quenching and of **I** decay, this range corresponds to the slow-exchange limit. (ii) Progress curves exhibiting two maxima (*2H*) arise only in a rather narrow "transition" range of K_a, 10^6 M$^{-1} > K_a > 10^4$ M^{-1}, which is explored in finer detail in Figure 12, lower. At the

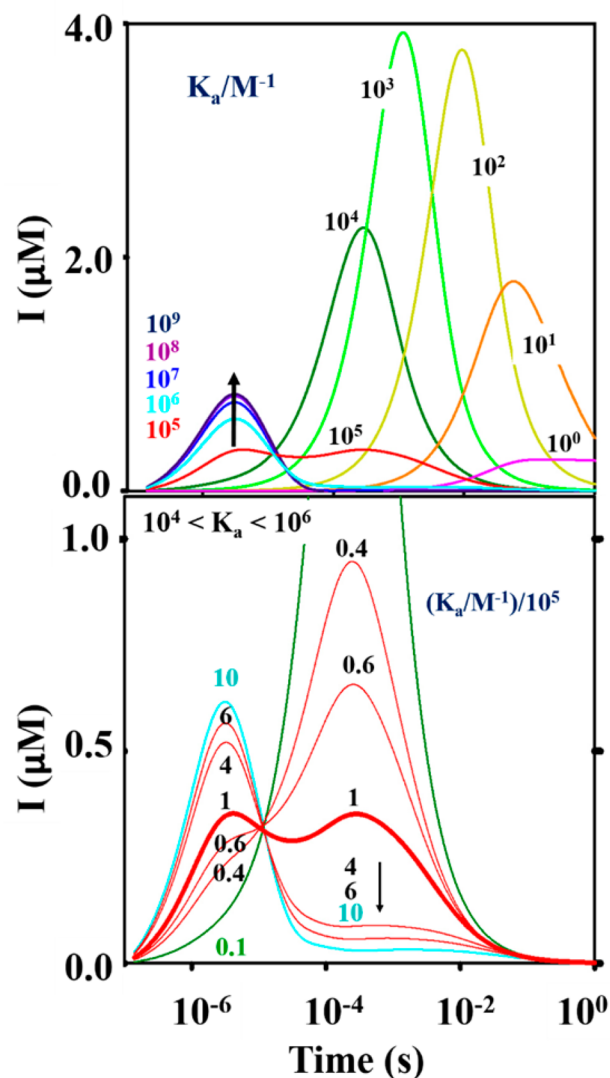**Figure 12.** Simulations of Scheme 1 with ET rates $k_q = 1.0 \times 10^5$ s^{-1} and $k_b = 8.0 \times 10^5$ s^{-1}, and [ZnDMb] = [Fe^{3+}Mb] = 10 μM held constant for each simulation. (Upper) K_a values were varied from 10^0 M^{-1} to 10^9 M^{-1} by changing k_{off} values; kon held constant at 10^9 M^{-1} s^{-1}. (Lower) Transition binding affinity range 10^4 M$^{-1} < K_a < 10^6$ M^{-1} where *2H* intermediates are observed. Red traces are labeled for $K_a = 4 \times 10^4$ M^{-1}, 6×10^4 M^{-1}, 1×10^5 M^{-1} ([ZnDMb(−6), Fe^{3+}Mb(+6)]), 4×10^5 M^{-1}, 6×10^5 M^{-1}. Green trace, 10^4 M^{-1}, Cyan trace 10^6 M^{-1}.

higher end of this range, when, 10^6 M$^{-1} > K_a > 10^5$ M^{-1}, the amplitude of the early time phase diminishes with decreasing K_a, and a long-time ($t \gtrsim 10^{-5}$ s) slow phase with a second order decay develops. Complexes in this K_a range predominantly undergo an intracomplex ET photocycle, but the moderate binding yields a small, but measurable, amount of unbound ^{3}ZnMb at 1:1 ratio, which reacts with free Fe^{3+}Mb ET partner which creates the second (slow) phase. In addition, small amounts of **I** dissociate and recombine in a slow second order process, adding to this second phase.

The amplitudes of the two maxima equalize at $K_a \sim 105$ M^{-1}, as observed here. At the lower end of the transition range, when 10^5 M$^{-1} > K_a > 10^4$ M^{-1}, the amplitude of the early time phase decrease with decreasing K_a and that of the slow phase increases (Figure 12, lower). In addition, the decay of the slow phase exhibits a more pronounced second order character as the amount of unbound ^{3}ZnMb becomes more prevalent, and
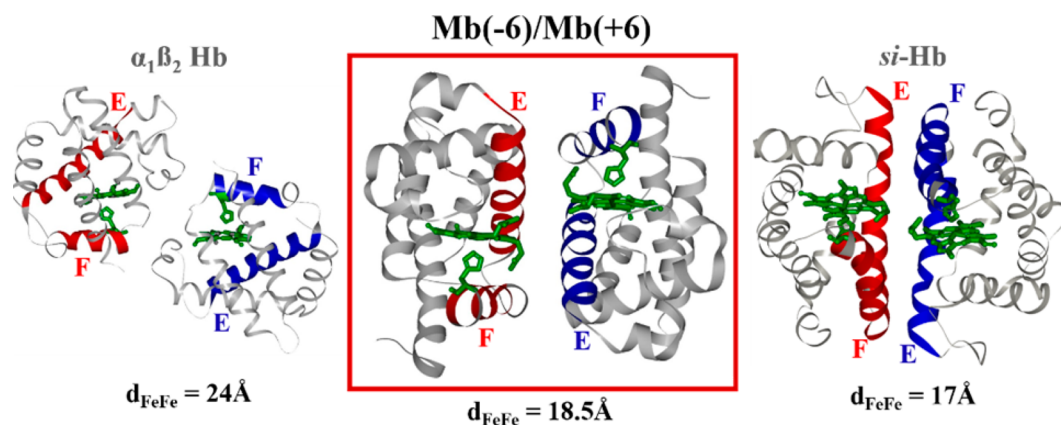
Figure 13. Globin assemblies for known high-affinity globins and a representative configuration for the [Mb(−6), Mb(+6)] complex. The E and F helices for the acidic partner (red) and the basic partner (blue) are indicated. Only the ET-active dimer is shown for the Hb.

the contribution from intracomplex ET diminishes. In parallel, dissociation of **I** formed by intracomplex ET occurs more frequently, and CR by the free components contributes to the second order "tail".

Finally, we note that *2H* progress curves for **I** exist only in this same overall range, $10^6 \text{ M}^{-1} > K_a > 10^4 \text{ M}^{-1}$, even when k_q, k_b have different values, and indeed when $k_q/k_b > 1$ (Figure S10), unlike the present case. What differs is only the details of the *2H* curves and their change with K_a.

(iii) As binding decreases below the transition limit, $K_a < 10^4$ M^{-1}, the ZnMb is almost completely free in solution under the low concentration conditions employed here. ET within a preformed complex thus becomes negligible, and both CS and CR become second order, a defining characteristic of the fast-exchange limit. In progress curves where $K_a < 10^4 \text{ M}^{-1}$, only a single long-time phase is observed, with a pseudo first-order appearance associated with the reaction of free ^{3}ZnMb with excess Fe^{3+}Mb, and decay through bimolecular CR; the amplitude of the progress curve reaches a maximum at $K_a \sim 10^{-3} \text{ M}^{-1}$, and decreases with further decrease in K_a. These calculations provide implicit validation of estimates for the binding constant for the Mb(WT) homodimer, $K_a < 5 \text{ M}^{-1}$ (Table 2). Indeed, visual inspection of Figure 9 shows that the timecourses for **I** in Mb(WT) complexes, with their low degree of maximal accumulation and slow decay are best reproduced when $K_a < 1 \text{ M}^{-1}$ in Figure 12, upper.

Figure 12 computationally traverses the spectrum of affinity constants from $K_a \sim 10^0 \text{ M}^{-1}$ to 10^9 M^{-1}, and experimenatially we have shifted the Mb-Mb affinity from $K_a \sim 10^0 \text{ M}^{-1}$ to $>10^5$ M^{-1} through the introduction of complementary surface-charge mutations that sharply increase qp. We note that one can "backslide" these binding advances by increasing the ionic strength, which weakens electrostatic binding. Indeed, test experiments have shown that the SE [ZnMb(−6), Fe^{3+}Mb-(+6)] complex transitions to a FE complex with increasing ionic strength. This change in kinetic landscapes is accompanied by *2H* → *1H* progress curve transitions, as predicted in Figure 12.

Viscosity Independent Intracomplex ET Kinetics Support the BD Predictions. The finding that the rate constants for intramolecular charge separation and charge recombination, k_q and k_b are independent of viscosity (or alternatively, osmotic pressure) indicates that these rate constants truly represent ET within a well-defined complex. This behavior is unique among investigations of interprotein

ET, where conformational "gating" that is modulated by viscosity/osmotic pressure has in fact been traditionally found.[40,44−50] The observation of such well-defined, viscosity independent intracomplex ET rate constants in turn matches with the prediction of a well-defined heterodimeric complex with a tight ensemble of structures (Figure 5). The small variations in ET rate constants that would arise in such an ensemble would be averaged to the single measured value by conformational interconversions that are fast compared to ET, even when slowed by the increase in viscosity. In short, the heterodimer behaves in a manner expected of a well-defined complex that approaches SD behavior (Figure 1).

The rate constants for photoinduced ET in the slow phase of the triplet decay and the corresponding "slow" component in the progress curve for **I** in [ZnMb(−6), Fe^{3+}Mb(+6)] are instead controlled by dynamic processes, as shown by their inverse dependence on solution viscosity (Figure 11). In the present case, the ET rates are slow enough to compete with dissociation, so the viscosity dependence is consistent with kinetic control by dissociation/association.

Monomer Assembly and Configurations from Brownian Dynamics. The tight binding of the charge-disproportionated heterodimer, together with its rapid, viscosity-independent intracomplex ET photocycle, confirm that the complex has a well-defined "structure", as predicted by the tight ensemble of conformations found in the BD simulation. We now consider in more detail the likely structure of this heterodimer, as implied by the surface contacts (Figure 6) and the distances/angles between the hemes (Figure 5), and compare them to known high-affinity globin assemblies. Figure 13 displays (left) the α_1/β_2 pair of Hb subunits (1DXU),[51] (right) the dimeric hemoglobin from clams (*Scapharca inequivalis*, *si*-Hb, 4SDH),[52,53] and (center) a representative [Mb(−6), Mb(+6)] configuration from the densest region of the BD contour plot for the heterodimer (Figure 5).

The protein−protein interface for the [Fe^{2+}Mb(−6), Fe^{3+}Mb(+6)] configuration in Figure 13, center, shows that the E and F-helices of the positively charged Fe^{3+}Mb(+6) (Figure 13, blue) are in "antiparallel" contact, respectively, with the F and E helices of the negatively charged Fe^{2+}Mb(−6) (Figure 13, red) giving facing heme edges, slightly offset, with a short metal−metal separation of $d_{Fe−Fe} \sim 18−19$ Å. This heterodimeric structure is remarkably similar to that of the homodimeric clam hemoglobin, which also has such an antiparallel interaction between E and F helices. This globin

assembly likewise has facing heme edges and short metal−metal separation ($d_{Fe−Fe}$ = 17 Å), and presumably would accommodate rapid ET (Figure 13, left). These two dimeric assemblies contrast with the α_1/β_2 pair of Hb subunits, where the interface does not involve the E and F helices and the heme edges are not well aligned; the closest metal−metal separation is 25 Å, which leads to slow intracomplex ET rates (~10^2 s$^{−1}$).[39,40] Indeed, even a domain-swapped MbMb homodimer, has a structure analogous to that of the Hb α_1/β_2 pair in that the heme faces (E and F helices) are not juxtaposed, and has an even longer metal−metal separation, 39.8 Å.[20]

NMR studies of the charge-disproportionated MbMb heterodimer will test its predicted structure (Figures 5, 13). A second round of BD simulations that begin with the heterodimer structure can identify additional pairs of surface sites where complementary charge-reversals can enhance binding and reactivity. The preparation of "supercharged" green fluorescent protein, with charges of +36 and −30,[54] suggests that electrostatic attractions can be further enhanced by adding even more charges to both the Mb(+6) and Mb(−6), while maintaining their structural integrity! To reach the highest affinities one may well need to incorporate shape complementarity, solvation, and hydrophic contacts.[55−58] However, it is not clear that higher-level approaches could take a weakly interacting Mb-Mb pair without a well-defined, known structure, and achieve the charge-disproportionated complex described here. In any case the present results showcase the exceptional utility of optimizing electrostatic interactions to enhance binding *and* reactivity through BD simulations.

SUMMARY

A refined BD interface redesign strategy led to the creation of a "charge-disproportionated" [Mb(−6), Mb(+6)] complex in which three K → E charge reversal mutations on the Mb(WT) surface generated a Mb(−6) mutant that binds to the positively charged Mb(+6) triple mutant. Analysis of the BD simulations with these two constructs predicted that they would form a well-defined, tightly bound heterodimeric complex with high intracomplex ET rate constants. In fact: (a) the binding affinity of the heterodimer is *no less than* 5 orders of magnitude greater than that of the Mb(WT) homodimer; (b) the intracomplex rate constants are also ~4 orders of magnitude greater than previously seen with mixed-metal Hb hybrids, and likely more than that for the WT Mb homodimer; (c) these rate constants are viscosity independent, suggesting they represent true interprotein ET, rather than dynamic gating as seen in all previous studies of interprotein photocycles.

We interpret these observations to support the conclusion that the charge-disproportionation strategy has indeed generated a tightly bound, ET-active heterodimer with high homology, which adopts a structure represented by that shown in Figure 13, and which approaches SD behavior (Figure 1). As a bonus, the CS intermediate, **I**, formed within this complex shows an unprecedented timecourse—accumulating to a maximum concentration, disappearing, then reappearing to a second maximum before finally vanishing. This behavior is explained by kinetic Scheme 1, which is general for protein−protein complexes.

ASSOCIATED CONTENT

Ⓢ Supporting Information

The Supporting Information is available free of charge on the ACS Publications website at DOI: 10.1021/jacs.6b07672.

> One BD figure, six crystallography figures and crystallography materials and methods, three crystallography tables, optical spectrum, and two kinetics figures. (PDF)

AUTHOR INFORMATION

Corresponding Author
*bmh@northwestern.edu

Present Addresses
§Institut für Physikalische Biologie, Heinrich-Heine-Universität Düsseldorf, Düsseldorf, 40255, Germany.
‖School of Applied Chemical and Environmental Sciences, Sheridan College, Brampton, Ontario L6Y 5H9, Canada.

Notes
The authors declare no competing financial interest.

REFERENCES

(1) Liang, Z.-X.; Nocek, J.; Huang, K.; Hayes, R. T.; Kurnikov, I. V.; Beratan, D. N.; Hoffman, B. M. *J. Am. Chem. Soc.* **2002**, *124*, 6849.
(2) Liang, Z.-X.; Kurnikov, I. V.; Nocek, J. M.; Mauk, A. G.; Beratan, D. N.; Hoffman, B. M. *J. Am. Chem. Soc.* **2004**, *126*, 2785.
(3) Nocek, J. M.; Hoffman, B. M. In *Encyclopedia of Biophysics*; Roberts, G. C., Ed.; Springer: New York, 2012; pp 534−537.
(4) Ubbink, M. *Biochem. Soc. Trans.* **2012**, *40*, 415.
(5) Volkov, A. N. *Acc. Chem. Res.* **2015**, *48*, 3036.
(6) Volkov, A. N.; Bashir, Q.; Worrall, J. A. R.; Ubbink, M. *J. Mol. Biol.* **2009**, *385*, 1003.
(7) Volkov, A. N.; Bashir, Q.; Worrall, J. A. R.; Ullmann, G. M.; Ubbink, M. *J. Am. Chem. Soc.* **2010**, *132*, 11487.
(8) Warshel, A.; Russell, S. T. *Q. Rev. Biophys.* **1984**, *17*, 283.
(9) Sharp, K. A.; Honig, B. *Annu. Rev. Biophys. Biophys. Chem.* **1990**, *19*, 301.
(10) Honig, B.; Nicholls, A. *Science* **1995**, *268*, 1144.
(11) Trana, E. N.; Nocek, J. M.; Knutson, A. K.; Hoffman, B. M. *Biochemistry* **2012**, *51*, 8542.
(12) Xiong, P.; Nocek, J. M.; Griffin, A. K. K.; Wang, J.; Hoffman, B. M. *J. Am. Chem. Soc.* **2009**, *131*, 6938.
(13) Nocek, J. M.; Knutson, A. K.; Xiong, P.; Co, N. P.; Hoffman, B. M. *J. Am. Chem. Soc.* **2010**, *132*, 6165.
(14) Xiong, P.; Nocek, J. M.; Vura-Weis, J.; Lockard, J. V.; Wasielewski, M. R.; Hoffman, B. M. *Science* **2010**, *330*, 1075.
(15) Trana, E. N., Ph.D. Dissertation. Northwestern University, 2014.
(16) Somireddy Venkata, B. K. R., Ph.D. Dissertation. Leiden University, 2012.
(17) Co, N. P.; Young, R. M.; Smeigh, A. L.; Wasielewski, M. R.; Hoffman, B. M. *J. Am. Chem. Soc.* **2014**, *136*, 12730.
(18) Royer, W. E., Jr. *J. Mol. Biol.* **1994**, *235*, 657.
(19) Van den Oord, A. H.; Wesdorp, J. J.; Van Dam, A. F.; Verheij, J. A. *Eur. J. Biochem.* **1969**, *10*, 140.
(20) Nagao, S.; Osuka, H.; Yamada, T.; Uni, T.; Shomura, Y.; Imai, K.; Higuchi, Y.; Hirota, S. *Dalton Trans.* **2012**, *41*, 11378.
(21) Evans, S. V.; Brayer, G. D. *J. Mol. Biol.* **1990**, *213*, 885.
(22) Keinan, S.; Nocek, J. M.; Hoffman, B. M.; Beratan, D. N. *Phys. Chem. Chem. Phys.* **2012**, *14*, 13881.

(23) Wheeler, K. E.; Nocek, J.; Cull, D. A.; Yatsunyk, L. A.; Rosenzweig, A. C.; Hoffman, B. M. *J. Am. Chem. Soc.* **2007**, *129*, 3906.

(24) Antonini, E.; Brunori, M. *Hemoglobin and Myoglobin in Their Reactions with Ligands*; North Holland Publishing Co.: Amsterdam, 1971.

(25) McCoy, A. J.; Grosse-Kunstleve, R. W.; Adams, P. D.; Winn, M. D.; Storoni, L. C.; Read, R. J. *J. Appl. Crystallogr.* **2007**, *40*, 658.

(26) Winn, M. D.; Ballard, C. C.; Cowtan, K. D.; Dodson, E. J.; Emsley, P.; Evans, P. R.; Keegan, R. M.; Krissinel, E. B.; Leslie, A. G.; McCoy, A.; McNicholas, S. J.; Murshudov, G. N.; Pannu, N. S.; Potterton, E. A.; Powell, H. R.; Read, R. J.; Vagin, A.; Wilson, K. S. *Acta Crystallogr., Sect. D: Biol. Crystallogr.* **2011**, *67*, 235.

(27) Lebedev, A. A.; Young, P.; Isupov, M. N.; Moroz, O. V.; Vagin, A. A.; Murshudov, G. N. *Acta Crystallogr., Sect. D: Biol. Crystallogr.* **2012**, *68*, 431.

(28) Laskowski, R. A.; Rullmannn, J. A.; MacArthur, M. W.; Kaptein, R.; Thornton, J. M. *J. Biomol. NMR* **1996**, *8*, 477.

(29) Adams, P. D.; Afonine, P. V.; Bunkoczi, G.; Chen, V. B.; Davis, I. W.; Echols, N.; Headd, J. J.; Hung, L. W.; Kapral, G. J.; Grosse-Kunstleve, R. W.; McCoy, A. J.; Moriarty, N. W.; Oeffner, R.; Read, R. J.; Richardson, D. C.; Richardson, J. S.; Terwilliger, T. C.; Zwart, P. H. *Acta Crystallogr., Sect. D: Biol. Crystallogr.* **2010**, *66*, 213.

(30) Vaguine, A. A.; Richelle, J.; Wodak, S. J. *Acta Crystallogr., Sect. D: Biol. Crystallogr.* **1999**, *55*, 191.

(31) Read, R. J.; Schierbeek, A. J. *J. Appl. Crystallogr.* **1988**, *21*, 490.

(32) Delano, W. L. *PyMOL*; Schrödinger: New York, 2002; http://www.pymol.org.

(33) The alternative charge reversals, to Asp rather than Glu, do not yield significantly different results.

(34) La Mar, G. N.; Budd, D. L.; Viscio, D. B.; Smith, K. M.; Langry, K. C. *Proc. Natl. Acad. Sci. U. S. A.* **1978**, *75*, 5755.

(35) La Mar, G. N.; Davis, N. L.; Parish, D. W.; Smith, K. M. *J. Mol. Biol.* **1983**, *168*, 887.

(36) Hoffman, B. M.; Celis, L. M.; Cull, D. A.; Patel, A. D.; Seifert, J. L.; Wheeler, K. E.; Wang, J.; Yao, J.; Kurnikov, I. V.; Nocek, J. M. *Proc. Natl. Acad. Sci. U. S. A.* **2005**, *102*, 3564.

(37) Fit of the fast phase of I to a binding isotherm (legend to Figure 10), indeed provided further conformation of this value.

(38) Smaller enhancements were observed with replacement of residues K78 and K87.

(39) Patel, A. D.; Nocek, J. M.; Hoffman, B. M. *J. Am. Chem. Soc.* **2005**, *127*, 16766.

(40) Patel, A. D.; Nocek, J. M.; Hoffman, B. M. *J. Phys. Chem. B* **2008**, *112*, 11827.

(41) Two species of camel have survived to modern times: Dromedary (1H), having one hump; Bactrian (2H), having two.

(42) Kuila, D.; Natan, M. J.; Rogers, P.; Gingrich, D. J.; Baxter, W. W.; Arnone, A.; Hoffman, B. M. *J. Am. Chem. Soc.* **1991**, *113*, 6520.

(43) Nocek, J. M.; Sishta, B. P.; Cameron, J. C.; Mauk, A. G.; Hoffman, B. M. *J. Am. Chem. Soc.* **1997**, *119*, 2146.

(44) Leferink, N. G.; Pudney, C. R.; Brenner, S.; Heyes, D. J.; Eady, R. R.; Samar Hasnain, S.; Hay, S.; Rigby, S. E.; Scrutton, N. S. *FEBS Lett.* **2012**, *586*, 578.

(45) Mei, H.; Wang, K.; Peffer, N.; Weatherly, G.; Cohen, D. S.; Miller, M.; Pielak, G.; Durham, B.; Millett, F. *Biochemistry* **1999**, *38*, 6846.

(46) Nocek, J. M.; Stemp, E. D. A.; Finnegan, M. G.; Koshy, T. I.; Johnson, M. K.; Margoliash, E.; Mauk, A. G.; Smith, M.; Hoffman, B. M. *J. Am. Chem. Soc.* **1991**, *113*, 6822.

(47) Nocek, J. M.; Liang, N.; Wallin, S. A.; Mauk, A. G.; Hoffman, B. M. *J. Am. Chem. Soc.* **1990**, *112*, 112.

(48) Zhou, J. S.; Kostic, N. M. *J. Am. Chem. Soc.* **1993**, *115*, 10796.

(49) Ivkovic-Jensen, M. M.; Kostic, N. M. *Biochemistry* **1997**, *36*, 8135.

(50) Schlarb-Ridley, B. G.; Mi, H.; Teale, W. D.; Meyer, V. S.; Howe, C. J.; Bendall, D. S. *Biochemistry* **2005**, *44*, 6232.

(51) Kavanaugh, J. S.; Rogers, P. H.; Arnone, A. *Biochemistry* **1992**, *31*, 8640.

(52) Royer, W. E., Jr.; Hendrickson, W. A.; Chiancone, E. *J. Biol. Chem.* **1989**, *264*, 21052.

(53) Nienhaus, K.; Knapp, J. E.; Palladino, P.; Royer, W. E., Jr.; Nienhaus, G. U. *Biochemistry* **2007**, *46*, 14018.

(54) Lawrence, M. S.; Phillips, K. J.; Liu, D. R. *J. Am. Chem. Soc.* **2007**, *129*, 10110.

(55) Kaufmann, K. W.; Lemmon, G. H.; DeLuca, S. L.; Sheehan, J. H.; Meiler, J. *Biochemistry* **2010**, *49*, 2987.

(56) Friedland, G. D.; Kortemme, T. *Curr. Opin. Struct. Biol.* **2010**, *20*, 377.

(57) Tyka, M. D.; Keedy, D. A.; Andre, I.; DiMaio, F.; Song, Y.; Richardson, D. C.; Richardson, J. S.; Baker, D. *J. Mol. Biol.* **2011**, *405*, 607.

(58) Palma, P. N.; Krippahl, L.; Wampler, J. E.; Moura, J. J. G. *Proteins: Struct., Funct., Genet.* **2000**, *39*, 372.